18

Three-Dimensional Microwave Imaging using Synthetic Aperture Technique

Shi Jun, Zhang Xiaoling, Yang Jianyu, Liao Kefei and Wang Yinbo
University of Electronic Science and Technology of China
Chengdu, P.R.China

1. Introduction

With the ability of two-dimensional (2-D) microwave imaging, synthetic aperture radar (SAR) has been an important imaging tool for civilian and military applications. The basic idea of 2-D SAR is to synthesize a linear array by moving a high-range-resolution (HRR) radar long a straight path, and obtain the additional azimuthal resolution. To exact the height information from the 2-D SAR, interferometric SAR (InSAR) technique, which requires multiple antennas or repeated flight paths, has been developed and is widely used for remote sensing applications.

However, since the interferometric SAR technique is based on the 2-D SAR images, it will be invalid, when there is more than one scatterer projected in the same pixel of the 2-D SAR image. This disadvantage makes it difficult to be used in high-precision 3-D RCS measurement and topographical survey in urban region.

To improve the ability of microwave remote sensing, some new 3-D SAR systems, such as circle SAR, elevation circular SAR, curve SAR, and linear array SAR have been developed based on the synthetic aperture technique. The basic idea of them is to produce 2-D resolution by moving the HRR radar in 2-D / 3-D space and obtain the third dimensional resolution using pulse compression technique. This chapter will discuss the principle and imaging processing technique of 3-D SAR.

In section 2, an approach to calculate the oscillatory integral has been introduced, which could simplify the analysis of 3-D SAR ambiguity function. In section 3, the ambiguity function and spatial resolution of 3-D SAR are discussed. The backprojection method and experiment data processing are presented in section 4 and 5 respectively. The multiresolution approximation techniques that can reduce the computational cost of 3-D SAR are discussed in section 6.

2. Preliminary

Compared with the traditional SAR, the echo model of 3-D SAR is more complex. To simplify the analysis of 3-D SAR, the calculation of oscillatory integral using density function will be introduced in this section.

2.1 A Simple Example

At first, let's observe a simple example. Assume that there is a discrete function $f(n) = (0,1/4,2/4,0,1/4,1/4)$, and we need to calculate the sum of $\exp(j \cdot 2\pi \cdot f(n))$. Obviously, we have:

$$\sum_n \exp(j \cdot 2\pi \cdot f(n)) = e^{j \cdot 2\pi \cdot 0} + e^{j \cdot 2\pi \cdot 1/4} + e^{j \cdot 2\pi \cdot 2/4} + e^{j \cdot 2\pi \cdot 0} + e^{j \cdot 2\pi \cdot 1/4} + e^{j \cdot 2\pi \cdot 1/4} \tag{1}$$

According to the commutative law of addition, eq. (1) can be rewritten as:

$$\sum_n \exp(j \cdot 2\pi \cdot f(n)) = 2 \cdot e^{j \cdot 2\pi \cdot 0} + 3 \cdot e^{j \cdot 2\pi \cdot 1/4} + 1 \cdot e^{j \cdot 2\pi \cdot 2/4} + 0 \cdot e^{j \cdot 2\pi \cdot 3/4} \tag{2}$$

where, coefficients 2, 3, 1 and 0 represent the frequency (in the sense of probability, which is defined as the number of times that value occurs in the data set) of every exponential term. Thus, by introducing the concept of density function $\mathcal{D}(i) = \{2,3,1,0\}$, we have:

$$\sum_n \exp(j \cdot 2\pi \cdot f(n)) = \sum_{i=0}^{3} \mathcal{D}(i) e^{j \cdot 2\pi \cdot i/4} . \tag{3}$$

Obviously, eq. (3) matches the definition of Discrete Fourier Transform (DFT). Denoting the DFT of $\mathcal{D}(i)$ as $\widehat{\mathcal{D}}(k)$, we have:

$$\sum_n \exp(j \cdot 2\pi \cdot f(n)) = \widehat{\mathcal{D}}(1) \tag{4}$$

Similarly, we have:

$$\sum_n \exp(j \cdot 2\pi \cdot k \cdot f(n)) = \sum_{i=0}^{3} \mathcal{D}(i) e^{j \cdot 2\pi \cdot k \cdot i/4} = \widehat{\mathcal{D}}(k) \tag{5}$$

This example indicates that the exponential sum of a finite discrete-time function can be calculated using its density function. However, since the commutative law of addition holds only when $f(n)$ is finite, and the concept of frequency is meaningful for finite set, a more precise definition of density function using Lebesgue measure and a theorem that extends eq. (4) to the continuous-time function will be presented in next subsection.

2.2 Calculation of the oscillatory integral using density function

According to measure theory, functions are divided into four classes, simple function, Bounded Function Supported on a set of Finite Measure (BFFM), non-negative function and integrable function (the general case). For the analysis of array whose size is finite, the BFFM assumption is sufficient.

Given a BFFM $f(t)$ with support $\boldsymbol{F}$, analogous to the definition of Cumulative Density Function (CDF) in probability theory, define the Cumulative Density Function of $f(t)$ as:

$$C_f(y) \triangleq m(\boldsymbol{F}_y) , \tag{6-1}$$

$$\boldsymbol{F}_y \triangleq \{t : f(t) \le y; y \in \mathbb{R}\}, \tag{6-2}$$

where, $\boldsymbol{F}_y$ is the subset of $\boldsymbol{F}$. $m(\boldsymbol{F}_y)$ denotes the Lebesgue measure of $\boldsymbol{F}_y$, which describe the volume (area) of $\boldsymbol{F}_y$. Especially, when $\boldsymbol{F}$ is finite set, $m(\boldsymbol{F}_y)$ is the cardinality of subset $\boldsymbol{F}_y$.

Then we define the Density Function (DF) of $f(t)$ as the derivative of $C_f(y)$:

$$\mathcal{D}_f(y) \triangleq dC_f(y)/dy \tag{7}$$

Obviously, $\mathcal{D}_f(y)$ satisfies:

1. $\mathcal{D}_f(y) \ge 0$;
2. $\int_{-\infty}^{+\infty} \mathcal{D}_f(y)dy = m(\boldsymbol{F}) < +\infty$;

Properties 1 and 2 of $\mathcal{D}_f(y)$ indicate that $\mathcal{D}_f(y)$ is absolutely integrable, and its Fourier transform exists.

Using the concept of density function, we can calculate an oscillatory integral using the following theorem.

Theorem 1: Given a BFFM phase function $f(t)$ supported on a set $\boldsymbol{E}$, we have:

$$\int_{\boldsymbol{E}} e^{jf(t)}dt = \widehat{\mathcal{D}}_f(1) \tag{8}$$

where, $\widehat{\mathcal{D}}_f(\bullet)$ denotes the Fourier transform of $\mathcal{D}_f(y)$

Proof:

The proof of theorem 1 includes two steps: firstly, we consider $f(t)$ as a simple function, and then extend the conclusion to BFFM function.

According to the definition in measure theory, a simple function is a finite sum of a group of characteristic functions:

$$f(t) = \sum_{k=1}^{K} a_k \chi_{\boldsymbol{E}_k}(t) \tag{9-1}$$

$$\chi_{\boldsymbol{E}_k}(t) = \begin{cases} 1 & t \in \boldsymbol{E}_k \\ 0 & t \notin \boldsymbol{E}_k \end{cases} \tag{9-2}$$

where, a_k is constant, $\boldsymbol{E}_k$ denotes a measurable subset of set $\boldsymbol{E}$, $\chi_{\boldsymbol{E}_k}(t)$ denotes the characteristic function of $\boldsymbol{E}_k$.

- Case 1: rational number

Assume that a_k are all rational number, there exists an equal-interval infinite rational number set:

$$\boldsymbol{B} = \{-\infty,...,\frac{-1}{Q},0,\frac{1}{Q},...,+\infty\}, Q \in \mathbb{N} \tag{10}$$

satisfying $a_k \in \boldsymbol{B}$ (in the example, $\{a_k\} = \{0,1/4,2/4\}$, $\boldsymbol{B} = \{0,1/4,2/4,3/4\}$).
Using set $\boldsymbol{B}$, we can construct a group of characteristic function $\chi_{\boldsymbol{F}_i}(t)$, and $f(t)$ could be written as:

$$f(t) = \sum_{i=-\infty}^{+\infty} b_i \chi_{\boldsymbol{F}_i}(t) \tag{11}$$

where, $b_i \in \boldsymbol{B}$; $\boldsymbol{F}_i = \boldsymbol{E}_k$, when $b_i = a_k$; otherwise, $\boldsymbol{F}_k = \Phi$.
According to the definition of Lebesgue integral, we have:

$$\int_{\boldsymbol{E}} e^{jf(t)} dt = \sum_{i=-\infty}^{+\infty} e^{jb_i} m(\boldsymbol{F}_i) = \sum_{i=-\infty}^{+\infty} e^{jb_i} \mathcal{D}_f(i) \tag{12}$$

Case 2: real number
Assume that a_k are all real number, according to the real analysis, for every real number a, there exists a sequence $\{a_n\}$ of rational numbers can approximate to it. Thus, there exists a sequence $\{\boldsymbol{B}_Q\}$ of rational number sets can approximate to all of the a_k, i.e.:

$$\int_{\boldsymbol{E}} e^{jf(t)} dt = \lim_{Q \to +\infty} \sum_{i=-\infty}^{+\infty} e^{jb_i^Q} \mathcal{D}_f^Q(i), \tag{13}$$

with the increase of Q, the interval $1/Q$ of $\boldsymbol{B}$ trends toward zero, and eq. (13) can be written in integral form as:

$$\int_{\boldsymbol{E}} e^{jf(t)} dt = \int_{-\infty}^{+\infty} e^{jy} \mathcal{D}_f(y) dy. \tag{14}$$

Since the Fourier transform of $\mathcal{D}_f(y)$ exists, we have:

$$\int_{\boldsymbol{E}} e^{jf(t)} dt = \widehat{\mathcal{D}}_f(1) \tag{15}$$

For a BFFM function $f(t)$ bounded by $\boldsymbol{M}$ and supported on a set $\boldsymbol{E}$, there exists a sequence $\{f_n\}$ of simples functions, with each f_n bounded by $\boldsymbol{M}$ and supported on a set $\boldsymbol{E}$, and such that:

$$f_n(t) \to f(t) \text{ for all } t. \tag{16}$$

Thus, eq. (8) holds for all BFFM functions.

□•

Theorem 1 provides a method to calculate the oscillatory integral without any approximation. Compared with the principle of stationary phase (PSP), this method does not need $f(t)$ be derivable, and holds for all BFFM function.

Using theorem 1, we can obtain the following corollary directly by rewritten eq. (12) as:

$$\int_E e^{j\cdot u\cdot f(t)}dt = \int_{-\infty}^{+\infty} e^{j\cdot u\cdot y}\mathcal{D}_f(y)dy = \widehat{\mathcal{D}}_f(u) \tag{18}$$

Corollary 1:

$$\int_E e^{j\cdot u\cdot f(t)}dt = \widehat{\mathcal{D}}_f(u) \tag{19}$$

As it will be seen in the next section, this corollary is crucial for the analysis on the ambiguity function of 3-D SAR.

3. Principle of 3-D SAR

3.1 Introduction on the typical 3-D SARs

In this subsection, a brief discussion on the typical 3-D SAR systems including circle SAR (CSAR), elevation circular SAR (E-CSAR), curve SAR, and linear array SAR (LASAR) will be proposed.

In 1999, Tsz-King Chan, Yasuo Kuga, and Akira Ishimaru proposed a novel method for radar topographical imaging which required the SAR platform to move in a circular orbit, and named it as circular SAR. In their experiment, the transmitting and receiving antennas were mounted on two separate wooden rings that were individually driven by stepping motors with an angular precision of approximately 0.02. Imaging result of a model helicopter of length 30 cm has been obtained and published (Tsz-King Chan; Kuga, Y.; Ishimaru, A., 1999). In 2001, at the Radar Division of Georgia Tech Research Institute (GTRI), a 3-D inverse synthetic aperture radar (SAR) system has been developed that performs synthetic aperture measurement via a linear motion of the radar in the elevation domain, and a circular (turntable) motion of the target in the range and cross-range domains, which was named as elevation circular SAR (E-CSAR) system. Its geometry is shown in Figure 1.

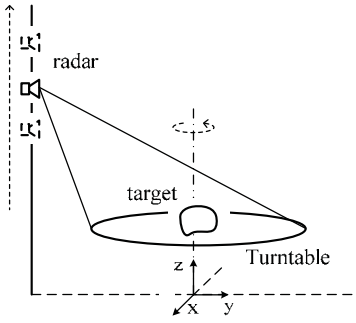

Fig. 1. Geometry of E-CSAR

The radar motion in elevation provides target coherent radar cross section (RCS) as a function of the elevation (or depression) angle. The target's circular motion yields the azimuthal look angle information. The imaging results of T-72 tank have been obtained and published (Bryant, M.L., Gostin, L.L., Soumekh, M. 2003). In fact, the concept "elevation circular SAR" could be extended by controlling the radar moving around the target in a helix trajectory which is shown in Figure 2. The cylindrical surface produces the 2-D resolution vertical (approximately) to the range resolution. Furthermore, to simplify the motion control, the helix trajectory could be composed by the circle motion of the radar and the rectilinear motion of the target, which is shown in Figure 3.

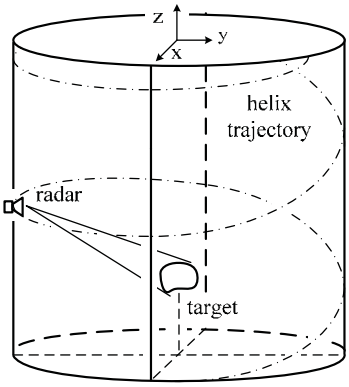

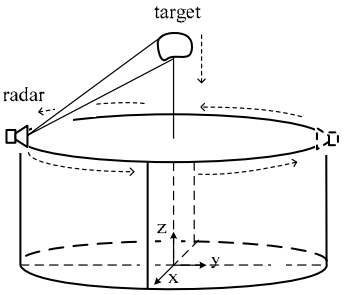

Fig. 2. Geometry of E-CSAR with helix trajectory Fig. 3. Geometry of E-CSAR composing helix trajectory by circle motion and rectilinear motion

The advantage of E-CSAR is that we can obtain the RCSes of the target in different elevation angle and azimuthal angle in one observation session; its disadvantage is that the target's size must be smaller than the diameter of the cylinder, which makes it difficult to be employed for large-size target. In fact, since the RCS of the target varies with the elevation angle and azimuthal angle, the synthetic aperture is a local region of the cylndrical surface, which is illustrated in Figure 4 (left).

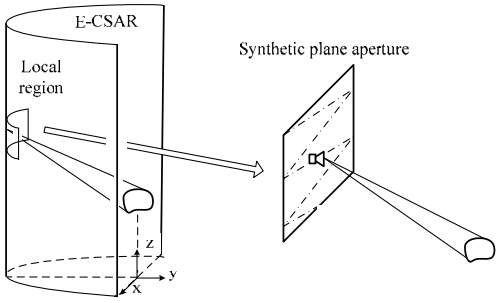

Fig. 4. Approximation of a local region of the E-CSAR using a synthetic plane aperture

Thus, we could approximate the local region as a plane and control the antenna phase centre moving in the plane by using a 2-D motion control platform or a linear array mounted on a 1-D motion control platform, which is shown in Figure 4 (right), and obtain the radar cross section (RCS) in one specific direction in one observation session. To obtain the RCSes in different elevation angle and azimuthal angle, one can just rotate the target or the platform. Compared with the E-CSAR, the size of the synthetic plane aperture is small and could be used in 3-D RCS measurement for large-size target.

Besides the E-CSAR, the curve SAR has also been researched in the radar community. In 1995, Jennifer L.H., Webb and David C. Munson, Jr. considered the problem of spotlight-mode synthetic aperture radar (SAR) imaging for an arbitrary radar path to reconstruct a 2-D image of 3-D surfaces. In 2004, Sune R. J. Axelsson researched the beam characteristics of 3-D SAR in curved or random paths in detail, and concluded that the SAR sidelobe suppression of a single circle path was worse than that of a circular antenna of similar size due to the fact that only a line boundary was used as SAR aperture. The spiral paths and random paths were discussed to improve the beam characteristic of 3-D SAR. The geometry of typical curve SAR is shown in Figure 5. The radar is mounted on a platform with curve path to synthesize a 2-D aperture.

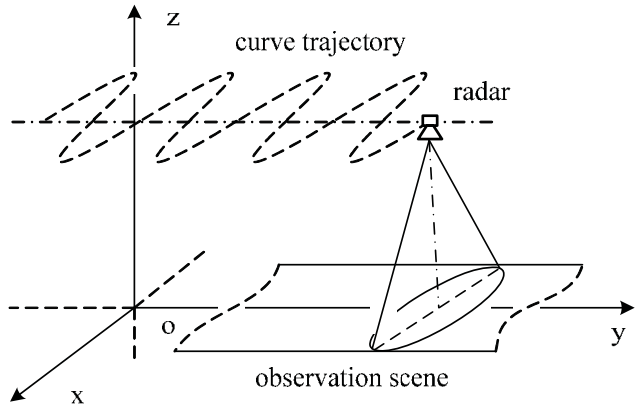

Fig. 5. Geometry of curve SAR

The advantage of curve SAR is that the size of the synthetic aperture could be far larger than the other 3-D SAR systems, which means high-resolution in the cross-track (x) direction; its disadvantage is that the motion control is too difficult to be implemented for the application of topographical survey in practice.

In 1996, Bassem R. Mahafza and Mitch Sajjadi proposed the concept "linear array SAR", which mounted a linear array on a platform with rectilinear motion and synthesized a 2-D plane array. Its geometry is shown in Figure 6. In 2004, R. Giret, H. Jeul and, P. Enert conceived a millimeter-wave imaging radar onboard an UAV, and designed a 3-D millimeter-wave imaging plan. In their plan, a linear array was mounted above the ground (perpendicular to the ground plane) and vehicles passed under the system to obtain the 3-D image of the vehicles.

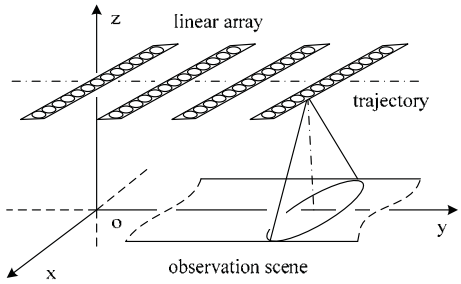

Fig. 6. Geometry of linear array SAR

Compared with the curve SAR, the motion control of linear array SAR is simpler. While, to achieve high cross-track resolution, the linear array must be rather long and the number of element is large, which is difficult and expensive to be implemented. To reduce the system complexity and cost, M. Weiß and J.H.G. Ender introduced the concept "MIMO radar" into the linear array SAR. With this concept, one can synthesize a sparse linear array SAR with relatively low cost, whose equivalent geometry is shown in Figure 7.

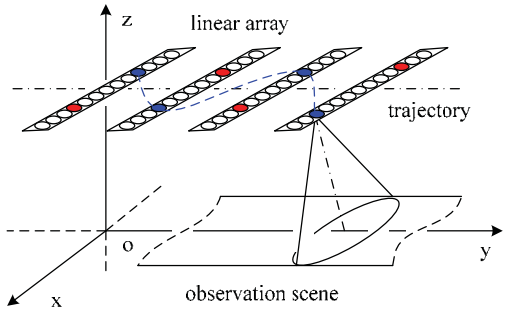

Fig. 7. Geometry of sparse LASAR, only the colored elements active at one pulse repetition period

The disadvantage of LASAR and sparse LASAR is that the cross-track resolution is determined by the length of the linear array. Since the length of the linear array is limited by the size of the platform, its cross-track resolution will be the bottleneck. Theoretically, the curve SAR could be considered as a kind of sparse LASAR (shown in Figure 7 in the blue dash-line).

In a word, the key problem of 3-D SAR is to vary the position of antenna phase centre (APC) in the 2-D / 3-D space. This work could be implemented mechanically (such as 2-D motion control platform and aircraft), or electrically (such as linear array). By moving HRR radar in 2-D plane using high precision motion control platform, we can build a low-cost 3-D RCS measurement device. The linear array SAR with MIMO technique might be the most feasible 3-D SAR system for the topographical survey application, thought there are still some problems, such as, the balance between the length of linear array and the cross-track resolution and the compensation of motion measurement error.

3.2 General echo model of 3-D SAR

For the traditional SAR, the echo is always considered as a function of fast-time τ and slow-time t. While, for 3-D SAR, there might be more than one channel echo received at one pulse repetition period, such as LASAR and sparse LASAR, and it is not convenient to describe the 3-D SAR echo using slow-time t. In fact, the synthetic aperture technique produces additional resolution by moving the antenna phase centre in the spatial domain, and we should pay more attention on the change of the antenna phase centre in spatial domain rather than that in the time domain. Thus, a general echo model is built in this subsection, which can describe different 3-D SAR systems.

Given a scatterer with position $\overline{\mathbf{P}}_{\omega}$, its slant range to the antenna phase centre with position $\overline{\mathbf{P}}_{apc}$ is:

$$R(\overline{\mathbf{P}}_{\omega}, \overline{\mathbf{P}}_{apc}) \triangleq \left\| \overline{\mathbf{P}}_{apc} - \overline{\mathbf{P}}_{\omega} \right\|_2 \tag{20}$$

where, $\|\bullet\|_2$ denotes the 2-norm of vector.

Given the transmitted baseband signal $f(t)$, ignoring the radiation pattern, the scatterer's echo $\mathcal{D}(\tau; \overline{\mathbf{P}}_{\omega}; \overline{\mathbf{P}}_{apc})$ can be written as:

$$\mathcal{D}(\tau; \overline{\mathbf{P}}_{\omega}; \overline{\mathbf{P}}_{apc}) = \exp(j \cdot 2\pi \cdot 2R(\overline{\mathbf{P}}_{\omega}, \overline{\mathbf{P}}_{apc})/\lambda) \cdot f(\tau - 2R(\overline{\mathbf{P}}_{\omega}, \overline{\mathbf{P}}_{apc})/c) \tag{21}$$

where, τ denotes the fast time domain, λ denotes the wave length of the carrier. The first term in eq.(21) is the Doppler term arising from the relative position changes of the antenna phase centre with respect to the target. The second term is the fast-time term which causes the range resolution. Note that, in some cases, the transmitter and receiver might be operated independently, and term $2R(\overline{\mathbf{P}}_{\omega}, \overline{\mathbf{P}}_{apc})$ in eq. (21) should be rewritten as $R(\overline{\mathbf{P}}_{\omega}, \overline{\mathbf{P}}^{T}_{apc})$ + $R(\overline{\mathbf{P}}_{\omega}, \overline{\mathbf{P}}^{R}_{apc})$, and the analysis should be modified correspondingly.

To describe the relative position changes, we introduce the concept "antenna phase centre set" $\mathbf{P}$ denoting the collection of the positions of the antenna phase centre (note that the elements in the antenna phase centre set might be repetitive.).

For traditional 2-D SAR, its antenna phase centre set could be expressed as:

$$\mathbf{P} = \{< x, y, z > \,|\, x = x_0, y = v \cdot t, z = z_0; t \in \mathbf{T}\} \tag{22}$$

where, v denotes the speed of the platform, $\mathbf{T}$ denotes the slow-time domain, z_0 denotes the height of the platform.

For E-CSAR, we have:

$$\mathbf{P} = \{< x, y, z > \,|\, x = \upsilon\cos(t), y = \upsilon\sin(t), z = v_h t; t \in \mathbf{T}\} \tag{23}$$

where, υ denotes the radius of the cylinder, v_h denotes the speed in the vertical direction.

For curve SAR, we have:

$$\mathbf{P} = \{< x, y, z > \left| x = x(t), y = v \cdot t, z = z_0; t \in \mathbf{T} \right.\} \tag{24}$$

where, $x(t)$ and $v \cdot t$ compose the curve trajectory.
For linear array SAR, we have:

$$\mathbf{P} = \{< x, y, z > \left| x \in \mathbf{X}, y = v \cdot t, z = z_0; t \in \mathbf{T} \right.\} \tag{25}$$

where, $\mathbf{X}$ denotes the set of the x positions of the linear array, e.g., $\mathbf{X} = \{x \left| i \cdot d; i = 0,1,...,N-1 \right.\}$, N denotes the element number of the linear array, d denotes the element interval.
For sparse LASAR, $\mathbf{P}$ is a group of random positions, and we just simplify denote it as $\mathbf{P}$.
Using the antenna phase centre set, we can easily express the echo of 3-D SAR as:

$$\mathbf{D}(r; \overline{\mathbf{P}}_\omega) = \{\mathcal{D} \left| \mathcal{D}(r; \overline{\mathbf{P}}_\omega; \overline{\mathbf{P}}_{apc}); \overline{\mathbf{P}}_{apc} \in \mathbf{P} \right.\} \tag{26}$$

Note that, given r, $\mathbf{D}$ is a set defined under the antenna phase centre set $\mathbf{P}$ rather than a number.
Thought this echo model is more abstract than the classical one, as it will be seen in the next subsection, it will simplify the analysis of 3-D SAR ambiguity function. We could build the direct relationship between the antenna phase centre set $\mathbf{P}$ (describes the shape of the synthetic aperture) and its ambiguity function, which make it easy for the 3-D SAR analysis and design.

3.3 Ambiguity function

Ambiguity function (AF) is one of the crucial concepts in the radar theory. For the pulse-Doppler (PD) radar, ambiguity function is a 2-D function of time delay and Doppler frequency. For imaging radar, it describes the interaction of different scatterers in the image space, which is also called point spread function. A well-designed imaging radar should have narrow mainlobe, low peak sidelobe ratio (PSLR) and low integrated sidelobe ratio (ISLR). In this section, we will discuss the ambiguity function of 3-D SAR.
Based on the echo model built in last subsection, the ambiguity function $\chi(\overline{\mathbf{P}}_\omega)$ of 3-D SAR can be defined as:

$$\chi(\overline{\mathbf{P}}_\omega) \triangleq \frac{\sum_{\mathbf{P}} \int \mathbf{D}(\tau; \overline{\mathbf{P}}_\omega) \cdot \mathbf{D}^*(\tau; \overline{\mathbf{0}}) d\tau}{\sum_{\mathbf{P}} \int \left| \mathbf{D}[\tau; \overline{\mathbf{0}}] \right|^2 d\tau} \tag{27}$$

where, superscript * denotes complex conjugate, $\overline{\mathbf{0}}$ denotes the position of the reference point.
Since the integration with respect to the fast time τ in eq. (27) is the range-compression operation, eq. (27) can be rewritten as:

$$\chi(\overline{\mathbf{P}}_\omega)=\frac{1}{M}\sum_{\mathbf{P}}\exp(j\cdot 2\pi\cdot[R(\overline{\mathbf{P}}_\omega,\overline{\mathbf{P}}_{apc})-R(\overline{\mathbf{0}},\overline{\mathbf{P}}_{apc})]/\lambda)\ \cdot\chi^R(r-2R(\overline{\mathbf{0}},\overline{\mathbf{P}}_{apc})) \quad (28)$$

where, r denotes the range domain, $\chi^R(r)$ denotes the ambiguity function in the range direction, which is a sinc function.

Approximating $\chi^R(r)$ as the impulse function, the range AF in eq.(28) could be moved out of the summation by range migration adjustment during imaging processing, and eq. (28) could be rewritten as:

$$\chi(\overline{\mathbf{P}}_\omega)\approx\frac{1}{M}\left\{\sum_{\mathbf{P}}\exp(j\cdot 2\pi\cdot[R(\overline{\mathbf{P}}_\omega,\overline{\mathbf{P}}_{apc})-R(\overline{\mathbf{0}},\overline{\mathbf{P}}_{apc})]/\lambda)\right\}\cdot\chi^R(r-2R(\overline{\mathbf{0}},\overline{\mathbf{P}}_0)) \quad (29)$$

where, $\overline{\mathbf{P}}_0$ denotes the centre of the synthetic aperture.

From eq.(29), the ambiguity function of 3-D SAR is the product of two terms: the first term in the curly brace is the Doppler term, which is caused by the synthetic aperture and produces resolution in the aperture direction(s); the second term is the fast-time term which produces range resolution. We define the synthetic aperture ambiguity function as:

$$\chi^{\mathbf{P}}(\overline{\mathbf{P}}_\omega)\triangleq\frac{1}{M}\left\{\sum_{\mathbf{P}}\exp(j\cdot 2\pi\cdot\Delta R(\overline{\mathbf{P}}_\omega,\overline{\mathbf{P}}_{apc})/\lambda)\right\} \quad (30)$$

$$\Delta R^{\omega}(\overline{\mathbf{P}}_{apc})\triangleq R(\overline{\mathbf{P}}_\omega,\overline{\mathbf{P}}_{apc})-R(\overline{\mathbf{0}};\overline{\mathbf{P}}_{apc})$$

where, $\Delta R^{\omega}(\overline{\mathbf{P}}_{apc})$ denotes the difference between $R(\overline{\mathbf{P}}_\omega,\overline{\mathbf{P}}_{apc})$ and $R(\overline{\mathbf{0}},\overline{\mathbf{P}}_{apc})$.

And the AF of 3-D SAR could be written as the product of $\chi^R(r)$ and $\chi^{\mathbf{P}}(\overline{\mathbf{P}}_\omega)$:

$$\chi(\overline{\mathbf{P}}_\omega)=\chi^{\mathbf{P}}(\overline{\mathbf{P}}_\omega)\cdot\chi^R(r-2R(\overline{\mathbf{0}},\overline{\mathbf{P}}_0)) \quad (31)$$

Eq (31) indicates that the AF of 3-D SAR could be divided as a range AF and a synthetic aperture AF and analyzed independently. Since the range AF is a sinc function and independent to the antenna phase centre set, $\chi^{\mathbf{P}}(\overline{\mathbf{P}}_\omega)$ should be paid more attention to.

For further analysis, we approximate $\Delta R^{\omega}(\overline{\mathbf{P}}_{apc})$ using the multivariable Taylor's theorem, and have:

$$\Delta R^{\omega}_{apc}\approx\overline{\mathbf{P}}_{apc}\cdot\overline{\mathbf{P}}^T_\omega/R(\overline{\mathbf{0}},\overline{\mathbf{P}}_0) \quad (32)$$

where, superscript T denotes the transpose operator.

Rewrite $\overline{\mathbf{P}}_\omega$ in the spherical coordinates as $\overline{\mathbf{P}}_\omega=\gamma\cdot\hat{\boldsymbol{\xi}}$, we have:

$$\Delta R^{\gamma\cdot\hat{\boldsymbol{\xi}}}_{apc}=\theta\cdot\overline{\mathbf{P}}_{apc}\cdot\hat{\boldsymbol{\xi}}^T \quad (33)$$

$$\theta=\gamma/R(\overline{\mathbf{0}},\overline{\mathbf{P}}_0)$$

where, γ denotes the radius of $\overline{\mathbf{P}}_{\omega}$, $\hat{\boldsymbol{\varsigma}}$ denotes the direction of $\overline{\mathbf{P}}_{\omega}$, θ is the ratio of γ to $R(\overline{\mathbf{0}},\overline{\mathbf{P}}_0)$.

Substituting eq. (33) into eq. (30), we have:

$$\chi_{\hat{\varsigma}}^{\mathbf{P}}(\theta)=\frac{1}{M}\cdot\sum_{\mathbf{P}}\exp\left[j\cdot 2\pi\cdot\theta\cdot(\overline{\mathbf{P}}_{apc}\cdot\hat{\boldsymbol{\varsigma}}^{T})/\lambda\right] \tag{34}$$

Regarding $(\overline{\mathbf{P}}_{apc}\cdot\hat{\boldsymbol{\varsigma}}^{T})/\lambda$ as a phase function, it is the projection of antenna phase centre set $\mathbf{P}$ onto the $\hat{\boldsymbol{\varsigma}}$ direction. Using corollary 1, we have the AF in the $\hat{\boldsymbol{\varsigma}}$ direction:

$$\chi_{\hat{\varsigma}}^{\mathbf{P}}(\theta)=\frac{1}{M}\cdot\int_{-\infty}^{+\infty}e^{j\cdot 2\pi\cdot\theta\cdot y}\mathcal{D}_{\hat{\varsigma}}(y)dy=\frac{1}{M}\cdot\widehat{\mathcal{D}}_{\hat{\varsigma}}(\theta) \tag{35}$$

The physical meaning of eq. (35) is shown in Figure 8. We can obtain the density function $\mathcal{D}_{\hat{\varsigma}}(i)$ by counting the number of elements whose projection on the $\hat{\boldsymbol{\varsigma}}$ direction is in the neighbourhood of i, and the AF in the $\hat{\boldsymbol{\varsigma}}$ direction is the Fourier transform of $\mathcal{D}_{\hat{\varsigma}}(i)$ approximately.

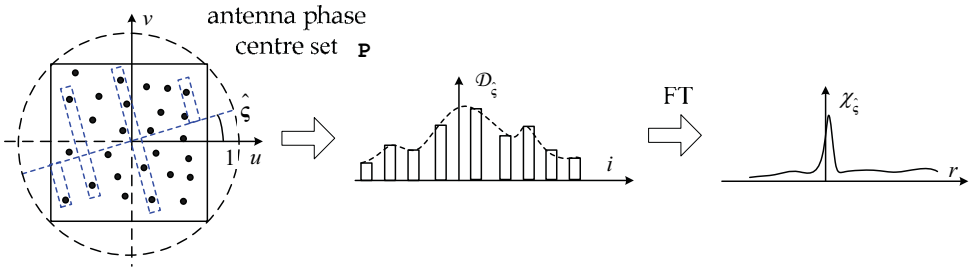

Fig. 8. Explanation on eq. (35), the AF in the $\hat{\boldsymbol{\varsigma}}$ direction is the Fourier transform of $\mathcal{D}_{\hat{\varsigma}}(i)$ approximately.

Eq. (35) builds the direct relationship between the antenna phase centre set $\mathbf{P}$ and the synthetic aperture ambiguity function $\chi_{\hat{\varsigma}}^{\mathbf{P}}(\theta)$. Then, the synthetic aperture ambiguity function of typical antenna phase centre sets will be discussed.

- **Z-shaped trajectory**

As a kind of simple continuous trajectory, Z-shaped trajectory is easy to be implemented using 2-D motion control platform and has been used in our experiments, which is shown in Figure 9-a. Figure 9-b and Figure 9-c are its ambiguity functions obtained by simulation and experiment respectively, and its grating lobe is high and dense.

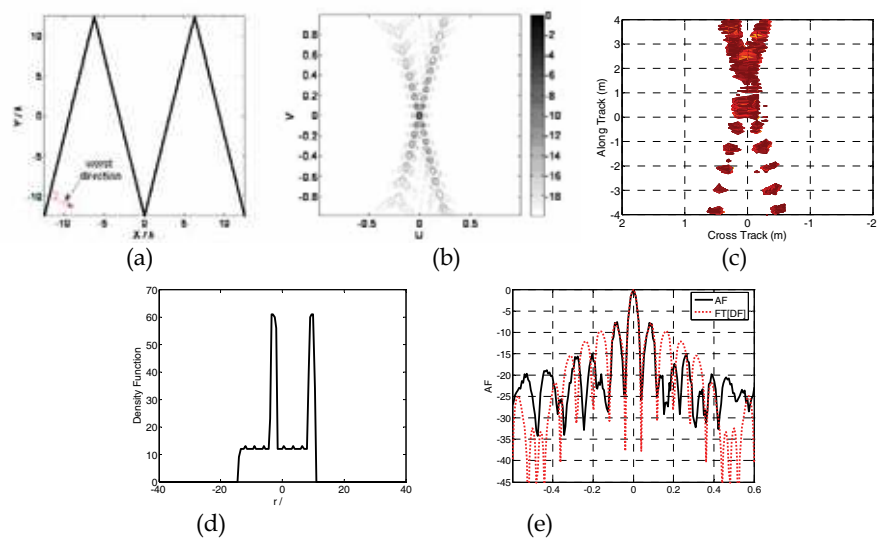

Fig. 9. (a) Z-shaped trajectory; (b) 2-D AF by simulation; (c) 2-D AF by experiment; (d) DF vertical to the edge, that two impulses are added on a rectangle function; (e) AF corresponding to Figure (d), whose grating lobes are quite high and dense.

This phenomenon could be explained using eq. (35). Observing Figure 9-a, we find that when the direction is vertical to the edge of the triangle function, all of the elements on one edge are projected on the same point, and there are two impulses are added on the density function (Figure 9-d). Consequently, the sidelobe of the directional AF (which is the Fourier transform of Figure 9-d and shown in Figure 6.e) is high, whose PSLR and ISLR are 7.60dB and -3.28 dB respectively.

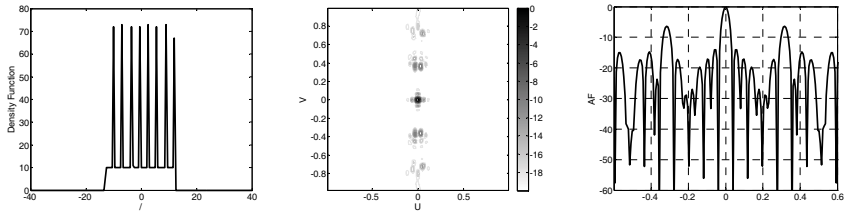

Fig. 10. (a) DF vertical to the edge with short period; (b) 2-D AF by simulation; (c) AF corresponding to Figure (a), whose grating lobes are sparse

High ISLR and PSLR mean that the sidelobe of strong scatterer will submerge the weak scatterer, and cause measurement error in the 3-D RCS measurement application. This problem could be solved by increasing the periodicity of the Z-shaped trajectory. With the increase of periodicity, the impulses in the density function increase correspondingly (Figure 10 a), and the grating lobe becomes sparse (Figure 10. b and c). Just as the grating lobe problem in the theory of antenna array, when the period of the Z-shaped trajectory is less than 1/2, the grating lobe will be eliminated completely.

- **Dense square array**

For LASAR, its synthetic aperture is a full-element square array, which is shown in Figure 11.a. Since the number of elements is equal for different x, its density function in the x direction is rectangle function, which is shown in Figure 11.b. The directional AF in the x direction is the Fourier transform of the rectangle function, which is a sinc function and shown in Figure 11.e. the black solid line is obtained by numerical simulation, the red dot line is the Fourier transform of Figure 11.b. The peak sidelobe ratio (PSLR) and integrated sidelobe ratio (ISLR) are -11.80 dB and -8.41dB respectively, which is near to the sinc function (-13.30 dB and -10.16 dB respectively).

Then, let's observe the density function in the diagonal direction. From Figure 11.a, it is obvious that the number of elements increases linearly from one endpoint of the diagonal to the centre, and decreases linearly from the centre to the other endpoint. In consequence, the density function in the diagonal direction is a triangle function, which is shown in Figure 11c. Figure 11 f is the AF in the diagonal direction. The black solid line is obtained by numerical simulation, the red dot line is the Fourier transform of Figure 11.c. The PSLR and ISLR are -22.86 dB and -20.71dB respectively, which is near to the Fourier transform of triangular window (-26.82dB and -22.02 dB respectively)

Figure 11.d is the 2-D AF of dense square array. We find that it has star-shaped AF.

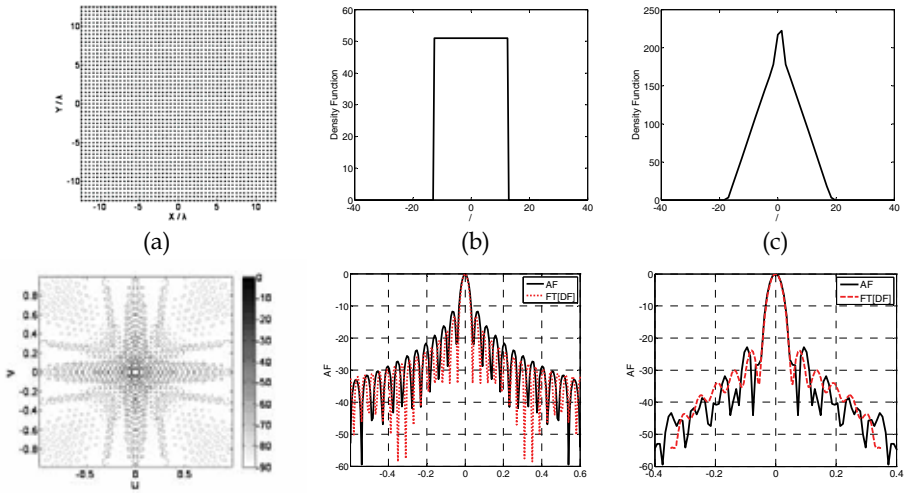

Fig. 11. (a) Dense square array; (b) DF in the x direction, which is a rectangle function; (c) DF in the diagonal direction, which is a triangle function; (d) 2-D AF of dense square array, whose sidelobes are distributed in the x and y directions mainly; (e) AF in the x direction, which is a sinc function; (f) AF in the diagonal direction, which is the Fourier transform of triangle function.

- **Random sampling**

For sparse LASAR, its synthetic aperture is a random sampling in the full-element square array, which is shown in Figure 12.a

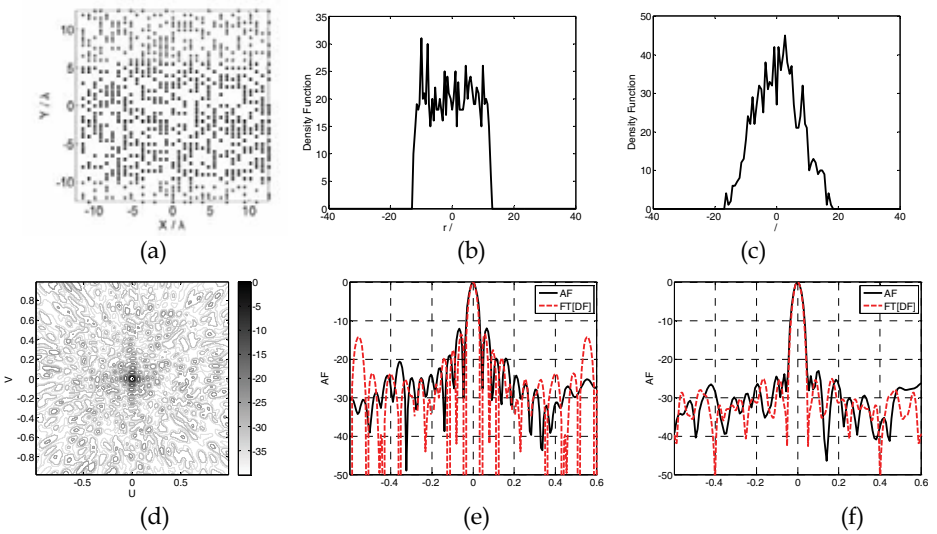

Fig. 12. (a) Random sampling square array; (b) DF in the x direction, which is a rectangle function with noise; (c) DF in the diagonal direction, which is a triangle function with noise; (d) 2-D AF; (e) AF in the x direction, which is similar to the Fourier transform of Figure b; (f) AF in the diagonal direction, which is similar to the Fourier transform of Figure c.

Figure 12. b and c are the density functions in the x and diagonal directions. Comparing with their counterparts of dense square array, we find that its density functions could be considered as the density functions of dense square array modulated by a noise. As a result, its PSLR in the x and diagonal directions (Figure 12.e and 12.f) are similar to those of dense square array. However, since the noise modulated on the density functions increases the high-frequency components, which are corresponded to the far-area sidelobes, its ISLR is higher than that of dense square array.

Figure 12.d is the 2-D AF of uniform distribution sparse array. Comparing with Figure 12.d, we find that its far-area sidelobe is higher than that of dense square array (Note the color bar). Energy leak is the main disadvantage of sparse array. One can improve the PSLR and ISLR by increasing the random sampling number, since its mainlobe energy is proportional to the square of the sampling number, and the sidelobe energy is proportional to the sampling number(Gauss distribution).

3.4 Spatial Resolution

The range resolution of 3-D SAR is produced by the pulse compression technique, and we can obtain the resolution formula directly as:

$$\rho_R = c/(2B) \tag{36}$$

where, c denotes the speed of light, B denotes the signal bandwidth.

The other two dimensional resolutions are produced using the array theory, and we can write the resolution formula as:

$$\rho = \lambda/(2\theta) \tag{37}$$

where, λ denotes the wave length, θ denotes the aperture angle. Remark that the "2" in eq. (37) indicates that the transmitter and receiver moving cooperatively. If the transmitter or receiver is fixed, the resolution formula should approximately be $\rho = \lambda/\theta$.

Note that, the aperture angle θ is influenced by the size of the array, the beam angle of the T/R antenna and the scatterer angle (the angle in which the RCS could be considered as constant.), which are shown in Figure 13.

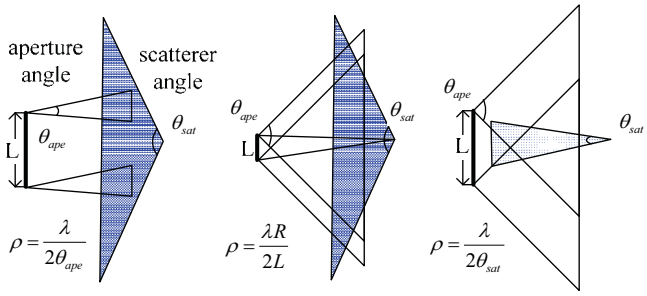

Fig. 13. Influenced of the array size, aperture angle and scatterer angle on the resolution

The resolution is restricted by the worst factor, i.e.:

$$\rho = \max\left(\frac{\lambda}{2\theta_{ape}}, \frac{\lambda R}{2L}, \frac{\lambda}{2\theta_{sat}}\right) \tag{38}$$

The first two factors could be optimized in the design of 3-D SAR system; the last factor arises from the scattering mechanism and is difficult to be reduced. It also means that we can not improve the resolution of 3-D SAR unlimitedly.

4. Backprojection Method

Backprojection (BP) algorithm is a 3-D SAR imaging algorithm based on the time domain correlation (TDC) technique, which coherently adds the data at the fast-time bin that corresponds to the location of a point for all synthetic aperture locations. The BP algorithm can be considered as the implementation of the definition of ambiguity function, and has been used in E-CSAR data processing.

The input of the BP operator is the raw data, antenna phase centre set and the scatterer's position; the output is the RCS of the scatterer.

Let $\mathbf{D}_{\mathrm{II}}$, $\mathbf{P}$ and $\overline{\mathbf{P}}_{\omega}$ be the raw data after range compression, antenna phase centre set and the scatterer's position, the BP operator can be expressed as:

$$\mathcal{C}[\mathbf{D}_{\mathrm{II}}, \mathbf{P}, \overline{\mathbf{P}}_{\omega},] \rightarrow \sigma_{\omega} \tag{39}$$

The implementation of the BP operator $\mathcal{C}[\bullet]$ is presented in eq. (40):

$$\mathcal{C}[\mathbf{D}_{\mathrm{II}},\mathbf{P},\overline{\mathbf{P}}_{uvw},] \triangleq \sum_{\mathbf{P}} \mathbf{D}_{\mathrm{II}} \cdot \exp(-j \cdot 2\pi \cdot 2R(\overline{\mathbf{P}}_{uvw},\overline{\mathbf{P}}_{apc})/\lambda) \cdot \chi^{R}(r-2R(\overline{\mathbf{P}}_{uvw},\overline{\mathbf{P}}_{apc}) \tag{40}$$

where, $\overline{\mathbf{P}}_{uvw}$ denotes the pixel in the image space.

From eq. (40), we know that just like the 2-D BP algorithm, the 3-D BP algorithm can roughly be divided into four steps: range-compression, interpolation, resampling and coherent summation, whose block diagram is shown in Figure 14. Processing the 3-D image region one pixel by one pixel, we can obtain the 3-D RCS distribution finally.

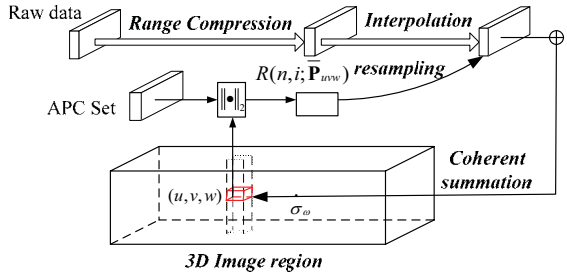

Fig. 14. Block diagram of 3D BP algorithm

From eq. (40), the computational cost $\Xi_{\mathcal{C}}$ of the single-scatterer compression operator $\mathcal{C}[\bullet]$ can easily be calculated as:

$$\Xi_{\mathcal{C}} = M \cdot (\Xi_{int} + \Xi_{coh}) \tag{41}$$

where, M denotes the total element number of antenna phase centre set, Ξ_{int} and Ξ_{coh} denote the computational costs of the interpolation operation and the coherent summation operation respectively.

Ignoring the computational cost of the range-compression operation, for a 3-D image region with size L• W• H(pixel^3), the total computational cost of 3-D BP algorithm is:

$$\Xi_{BP} = \mathrm{L} \cdot \mathrm{W} \cdot \mathrm{H} \cdot \Xi_{\mathcal{C}} \tag{42}$$

Compared with 2-D BP, there are two factors that cause the computational cost of 3-D BP algorithm is far larger than that of 2-D BP: the increase of the acquired data and the extension of image region. The former factor can partially be solved using the sparse array technique. The latter factor can be solved using the multiresolution approximation technique, which will be introduced in the following section.

5. Imaging Processing of 3-D SAR

To verify the feasibility of "one-active" LASAR, a series of experiments have been carried out. The typical experiment plan is shown in Figure 15, and includes three parts: "one-active" LASAR, reference points and scene area.